Journal of Materials Chemistry C

Accepted Manuscript

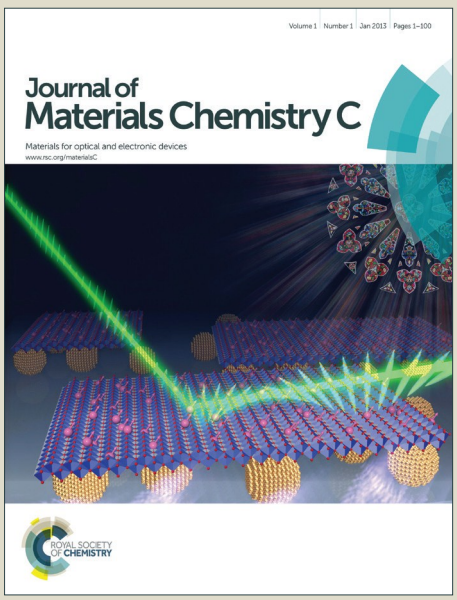

ROYAL SOCIETY OF CHEMISTRY

www.rsc.org/materialsC

"Scorpion" shape mono (carboxy)Porphyrin-(Bodipy)$_2$: a novel triazine bridged triad, synthesis, characterization and its dye sensitized solar cell (DSSC) applications

Zervaki E. Galateia[1], Nikiforou Agapi[1], Nikolaou Vasilis[1], Ganesh D. Sharma[2*], Coutsolelos G. Athanassios[1*]

[1]Laboratory of Bioinorganic Chemistry, Department of Chemistry, University of Crete, Voutes Campus, P.O. Box 2208, 71003 Heraklion, Crete, Greece

[2]R&D Center for Engineering and Science, JEC Group of Colleges, Jaipur Engineering College, Kukas, Jaipur (Raj.) 303101, India

KEYWORDS: DSSC, porphyrin triad, triazine, BODIPY, reduced graphene oxide

Corresponding authors: coutsole@chemistry.uoc.gr, gdsharma273@gmail.com

Abstract

A novel BODIPY-porphyrin triad **PorCOOH-(BDP)$_2$** (scorpion shape) prepared, where two Bodipy molecules are covalently attached via a 1,3,5-triazine molecule on a free-base carboxyphenyl meso-substituted porphyrin. The chromophore synthesized *via* stepwise substitution reactions of cyanuric chloride. Photophysical and electrochemical studies of this triad, in combination with DFT theoretical calculations, suggest that there is negligible electronic interaction between the porphyrin and BODIPY moieties in the triad's ground states, but the frontier orbital energy levels are suitable for use as sensitizers in dye-sensitized solar cells (DSSCs). Solar cells sensitized by triad **PorCOOH-(BDP)$_2$** fabricated, and found to exhibit a power conversion efficiency (PCE) value of 5.17%, under illumination (AM1.5, 100 mW cm^2), and TiO_2 films of 12 μm thickness, with sensitization time of 3 hr without any coadsorbent. The PCE value of DSSC was enhanced up to 6.20%, when a thin layer of reduced graphene oxide (rGO) was incorporated between TiO_2 and **PorCOOH-(BDP)$_2$** dye, which is attributed to the formation of rGO-TiO_2 Schottky barrier in the device, leading to efficient charge transport of injected electrons towards the external circuit, resulting in higher J_{sc} and FF. Electrochemical impedance spectra (EIS) demonstrate that with rGO-TiO_2 photoelectrode exhibits shorter transport time of electron, longer electron lifetime of electron and lower charge transfer resistance.

Introduction

Dye sensitized solar cells (DSSCs), first reported by Grätzel in 1991, have attracted a lot of attention due to their low cost fabrication and high power conversion efficiency (PCE) values, in the aim of developing and improving the renewable energy sources.[1] A typical DSSC is constituted of a dye sensitized TiO_2 electrode, a Pt counter electrode, and an electrolyte. The sensitizer plays an important role in the PCE value of DSSC. A dye, which is anchored to the surface of the TiO_2 nanocrystalline electrode, absorbs the solar radiation and transfers the photoexcited electron to the conduction band of the TiO_2. In this respect, many sensitizers with donor-π-acceptor (D-π-A) configurations have been developed.[2] Among them, porphyrins have been used as sensitizers for DSSCs due to their strongly absorbing Soret band (λ=400 – 450 nm) and moderately intense Q bands (λ=550 – 650 nm), which cover the visible to near infrared (NIR) region of solar spectrum.[3] Moreover, their optical and electrochemical properties can be tuned easily by simple modification of their chemical structure. Recently, Diau and Yeh *et al*. designed a highly efficient porphyrin sensitizer, functionalized with two bis-(ortho-alkoxy)-wrapped meso-phenyl groups for reducing dye aggregation, and an ethynyl benzoic acid group as the acceptor.[4] More recently, highest efficiency values of 13.0% and 12.75% on DSSCs, sensitized with porphyrins which have octyloxy-wrapped structures, utilizing a benzothiadiazole bridge between the ethynyl and benzoic acid moieties and using a cobalt based electrolyte, have been reported by Grätzel and co-workers.[5]

Although the absorption spectrum of porphyrins is strong in Soret and moderate in Q band regions, it exhibits poor absorption intensity in the region between 475 nm to 550 nm. To compensate this poor absorption intensity of porphyrin several research groups have investigated dyes in that region, extended π-systems in porphyrins. This approach can lead to significant broadened Soret band and red shift Q band absorption peaks. For example, elongation of π-systems in *meso*- and β-naphthalene fused-porphyrins improves the PCE value by 50%, in comparison with the non-fused systems.[6] Similarly, attaching a conjugated anchoring group at the β-position of the porphyrin ring has been successfully applied and the DSSC based on this porphyrin dye yielded a PCE value of 7.1%.[7]

One of the approaches for improving the absorption properties of porphyrin derivatives in the region of 450–550 nm is their linking with chromophores that strongly absorb in the above region. BODIPY fluorophores have been widely used as light harvesting antenna groups, whose derivatives had excellent photochemical properties with strong absorption bands from the visible to NIR region[8] and possess complementary properties with porphyrins. Moreover, recently, Ziessel *et al.* reported a PCE value of 5.75% for the DSSCs using BODIPY dyes.[9] Also, molecules consist of both porphyrin and BODIPY chromophores have been developed to enhance the optoelectronic properties of resulting molecules.[10] Some strategies were developed for improving the limited photophysical profile of porphyrin derivatives in the blue green region of the spectrum. So, porphyrins were modified with BODIPY as antenna chromophore for efficient intramolecular energy transfer.[10b, 11] A BODIPY-porphyrin conjugate, with an acetylide group as a bridge, has recently shown improved PCE value, compared to its parent porphyrin chromophore when used as a sensitizer in a DSSC.[12] Lazarides and co-workers designed multi-chromophore arrays consisting of two BODIPY units, axially bound to porphyrin complexes, which have been investigated for electron or energy transfer mechanism. Among all chromophore groups, one of the most effective light harvesting efficiency values was achieved by using a phenolate group as a linker.[13]

1,3,5-triazine moiety has been used as a linker for the synthesis of metal free organic dyes as sensitizers for DSSCs and other photoconductive materials.[14] The structural, chemical and electronic properties of this unit allow the synthesis of complex π-conjugated multi-chromophores dyes through simple organic reactions[15] that offer improved light harvesting ability, as well as improved electron injection and transportation rates.[16] Triad compounds where triazine moiety is covalently connected with a BODIPY moiety have been synthesized and their fluorescent properties are studied.[15b,c] Liu *et al.* reported a solar cell, sensitized by a triazine-based metal-free organic dye with a D–π–A structure, that showed a PCE value of 3.63%.[17] Triazine–bridge porphyrin arrays have been used as electron donors in bulk heterojunction (BHJ) solar cells by Luechai *et al.*[18] and recently by us.[19] In addition, our research group synthesized a series of triazine bridged porphyrin dyads and triad and DSSCs based on these sensitizers showed moderate PCE values.[20]

In this work, we describe a facile synthesis of BODIPY-porphyrin triad [**PorCOOH-(BDP)$_2$**], using a triazine linker, and its application as sensitizer for DSSCs. The DSSC based on that BODIPY-porphyrin triad attached onto TiO_2/FTO photoelectrode showed a PCE value of 5.17%, which was further improved up to 6.20% when rGO/TiO_2/FTO (rGO means reduced graphene oxide) photoelectrode was used. The increase in the PCE value was attributed to the more efficient transport of injected electrons towards the FTO surface, due to the formation of a Schottky barrier formed between rGO and TiO_2.

Experimental details

General methods, materials, and techniques. All manipulations were carried out using standard Schlenk techniques under nitrogen atmosphere. 2,4,6-Trichloro-1,3,5-triazine (cyanuric chloride), diisopropylethylamine (DIPEA) and other chemicals and solvents were purchased from usual commercial sources and used as received, unless otherwise stated. Tetrahydrofuran (THF) was freshly distilled from Na/benzophenone. 4-Aminophenyl-4,4-difluoro-4-bora-3a,4a-diaza-s-indacenes (or 4-aminophenyl-boron dipyrrin or NH_2-BDP) and 5-(4-carboxyphenyl)-15-(4-aminophenyl)-10,20-bis(2,4,6-trimethylphenyl)-porphyrin (PorCOOH) were prepared according to literature procedures.[21, 22]

Synthesis of triad PorCOOH-(BDP)$_2$ (3): To a THF solution (2 mL) of cyanuric chloride (0.0098 g, 0.053 mmol) and DIPEA (11 μL, 0.064 mmol) a THF solution (2 mL) of porphyrin PorCOOH (0.040 g, 0.053 mmol) was added, under N_2 at 0^{o}C. The mixture was stirred at 0^{o}C for 15 min, and upon reaction completion (monitored by TLC), it was left to warm at room temperature. Next, a THF solution (4 mL) of NH_2-BDP (0.027 g, 0.08 mmol) and DIPEA (22 μL, 0.128 mmol) was added and the mixture was stirred at room temperature overnight. Another excess of NH_2-BDP (0.090 g, 0.265 mmol) and

DIPEA (92 μL, 0.53 mmol) were added and the mixture was stirred at 65°C for 24h. The volatiles were removed under reduced pressure and after dilution in CH_2Cl_2; the residue was purified by column chromatography (silica gel, CH_2Cl_2). The desired product **3** was isolated as a purple solid. Yield: 0.038 g (47.4%). ^{1}H NMR (500 MHz, $CDCl_3$): δ_H (ppm) 8.75 (*m*, 8H), 8.63 (*d*, *J* = 8.5 Hz, 1H), 8.54 (*t*, *J* = 8 Hz, 2H), 8.48 (*d*, *J* = 8 Hz, 1H), 8.41 (*d*, *J* = 8.5 Hz, 1H), 8.37 (*d*, *J* = 8.5 Hz, 2H), 8.24 (*m*, 2H), 8.07 (*d*, *J* = 8 Hz, 1H), 7.92 (*s br*, 2H), 7.30 (*m*, 6H), 7.24 (*m*, 2H), 5.95 (*s br*, 4H), 2.64 (*s*, 6H), 2.55 (*m*, 6H), 1.85 (*s*, 12H), 1.42 (*m*, 12H), 1.26 (*s*, 6H), -2.62 (*s*, 2H). ^{13}C NMR (75 MHz, $CDCl_3$): δ_C 171.1, 155.7, 149.4, 147.8, 143.2, 139.7, 138.6, 138.1, 135.3, 134.7, 131.1, 129.1, 128.7, 128.1, 125.1, 122.0, 121.3, 119.0, 116.5, 32.4, 29.9, 26.6, 23.7, 21.9, 21.7; HRMS (MALDI-TOF): *m/z* calcd for $C_{92}H_{83}B_2F_4N_{14}O_2$, 1513.6867 $[M+H]^+$: found 1513.6951. UV-vis (CH_2Cl_2), λ / nm ($\varepsilon \times 10^{-3}$ / M^{-1} cm^{-1}): 420 (351.2), 502 (10.2), 550 (9.6), 592 (5.9), 650 (7.0). Anal. Calcd for $C_{92}H_{82}B_2F_4N_{14}O_2$: C, 73.02; H, 5.46; N, 12.96. Found: C, 73.08; H, 5.64; N, 12.47.

NMR spectra. ^{1}H NMR spectra were recorded on a Bruker AMX-500 MHz and ^{13}C NMR spectra on Bruker DPX-75 MHz spectrometer, as solutions in deuterated solvents by using the solvent peak as the internal standard.

Mass spectra. High-resolution mass spectra were recorded on a Bruker UltrafleXtreme MALDI-TOF/TOF spectrometer.

FTIR spectra. FTIR spectra were recorded on a Perkin Elmer 16PC FTIR spectrometer.

Photophysical measurements. UV-vis absorption spectra were measured on a Shimadzu UV-1700 spectrophotometer using 10 mm path-length cuvettes. Emission

spectra were measured on a JASCO FP-6500 fluorescence spectrophotometer equipped with a red sensitive WRE-343 photomultiplier tube (wavelength range: 200-850 nm). Emission lifetimes were determined by the time-correlated single-photon counting technique using an Edinburgh Instruments mini-tau lifetime spectrophotometer equipped with an EPL 405 pulsed diode laser at 406.0 nm with a pulse width of 71.52 ps and pulse periods of 50 ns and a high-speed red sensitive photomultiplier tube (H5773-04) as detector.

Electrochemistry measurements: Cyclic and square wave voltammetry experiments were carried out at room temperature using an AutoLab PGSTAT20 potentiostat and appropriate routines available in the operating software (GPES, version 4.9). Measurements were carried out in freshly distilled and deoxygenated CH_2Cl_2, with scan rate 100 mV/s, with a solute concentration of 1.0 mM in the presence of tetrabutylammonium hexafluorophosphate (0.1 M) as supporting electrolyte. A three-electrode cell setup was used with platinum working electrode, a saturated calomel (SCE) reference electrode, and a platinum wire as counter electrode. The system was calibrated by ferrocene.

Computational methods: All the theoretical calculations were performed using Gaussian 03 program suite.[23] Density functional theory (DFT)[24] with hybrid B3LYP functionals[25,26] and the 6-31G(d) basis sets were used for gas phase geometry optimization of **PorCOOH-(BDP)$_2$** (Figure 6, Table S1, Supporting Information). TDDFT calculations were carried out using geometry optimized coordinates in same level of theory and basis sets. Tomasi's Polarizable Continuum Model (PCM)[27] was used for describing the solvent effect (dichloromethane) with standard dielectric constant ε =

8.93. The input geometries as well as the computed structures and molecular orbitals were modeled using ChemCraft software.[28]

Device fabrication and characterization

The working and counter electrodes consisted of TiO_2 and thermally platinum films, respectively, were deposited onto F-doped tin oxide (FTO) conducting glass substrates which were pre-cleaned with deionized water, acetone, and ethanol and then dried in air. For the working electrode, TiO_2 paste, prepared as reported earlier[20], was deposited on the FTO substrate by the doctor blade technique. TiO_2 films of different thicknesses were prepared (4, 6, 8, 10, and 12 μm) in order to optimize the photovoltaic performance of DSSCs. In all cases, the electrode was sintered at 450 °C for 30 min. After cooling to room temperature, it was immersed in a 20 mM $TiCl_4$ aqueous solution for 30 min at 80 °C, washed with deionized water and ethanol, sintered again at 450 °C for 30 min, and cooled at 60 °C. Graphene oxide (GO) was prepared from the graphite powder according to a two-step oxidation protocol reported by Kovtyukhova et al [29]. For reduction of GO, the thermal treatment method was adopted. A 0.5 mg GO was first dispersed in 2 mL ethanol followed by ultrasonic treatment for 1 hr to yield the yellow brown solution. For the preparation of rGO/TiO_2/FTO photoanode, above prepared GO was spin coated with an aqueous solution of GO on the top of above prepared TiO_2/FTO electrode for 30 s at rpm of 2500 and then heated at 120 °C for 20 min, in ambient air. The GO is converted into reduced graphene oxide (rGO) through the hydrothermal treatment. Finally, the photoelectrode i.e. TiO_2/FTO or rGO/ TiO_2/FTO was immersed in a porphyrin solution (200 μM in THF for different immersing time periods) to give the porphyrin-sensitized TiO_2 working electrode. The platinum counter electrode was prepared by spin-coating drops of a H_2PtCl_6 solution onto a FTO-coated glass substrate and heating at 350 °C for 15 min. Separating the working electrode from the counter electrode by a 20-μm-thick Surlyn hot-melt gasket assembled the DSSCs. In the space between the working and counter electrodes, the electrolyte [consisting of 0.05 M I_2, 0.5 M LiI, 0.6 M (dimethylpropyl)-benzoimidiazole iodide, 0.5 M 4-tert-butylpyridine in an acetonitrile solution] was introduced through a hole and sealed with Surlyn. The devices

prepared with TiO_2/FTO and rGO/TiO_2/ FTO were denoted as device A and device B, respectively.

The current-voltage (J−V) characteristics of the DSSCs under illumination were measured by a Keithley source meter and a solar simulator coupled with a 150 W xenon lamp and an AM optical filter to give 100 mW/cm^2 illumination at the DSSC surface. The EIS spectra, in the dark and under illumination, were recorded using an electrochemical workstation (Autolab PGSTAT) with a frequency response analyzer. The frequency range was from 10 mHz to 100 kHz, and an alternative-current potential of 10 mV was used. A direct-current bias equivalent to the open-circuit voltage of DSSC was applied. The impedance data were analyzed using Z-View software with an appropriate equivalent circuit. The IPCE value was measured as a function of the wavelength with a xenon lamp, a monochromator, and a Keithley source meter under constant illumination intensity at each wavelength. The intensity calibration for the IPCE measurement was performed using a standard silicon photo-diode.

Results and discussion

Synthesis and characterization

As shown in Scheme 1, the porphyrin triad PorCOOH-(BDP)$_2$ **(3)**, consists of a *meso* aryl-substituted free-base porphyrin unit PorCOOH (namely 5-(4-carboxyphenyl)-15-(4-aminophenyl)-10,20-bis(2,4,6-trimethylphenyl)porphyrin) and two bodipy units, abbreviated as NH_2-BDP, which are connected, through aryl-amino groups at their peripheries, by a central 1,3,5-triazine moiety. Specifically, the choice of that porphyrin unit was led by the fact that the sterically demanding mesityl moieties, presented as substituents in the 10,20- *meso* positions, exhibit the ability to afford *trans-meso* substituted porphyrins without scrambling, thus avoiding the formation of a complicated mixture of porphyrins.[22] Also, the porphyrin moiety contains an anchoring group for the attachment onto TiO_2 surface of DSSC electrodes.

The synthesis of the triad, shown in Scheme 2, was accomplished via stepwise amination reactions of cyanuric chloride, which is the precursor of the bridging 1,3,5-triazine group of the triad. The potential of cyanuric chloride to provide access to a variety of triazine-bridged assemblies, such as macrocycles,[30] dendrimers,[31] and multiporphyrin arrays,[21,32] has been demonstrated in the past. Furthermore, we have recently reported symmetrical and unsymmetrical triazine-bridged porphyrin dyads and triads.[Error! Bookmark not defined.,Error! Bookmark not defined.]

The initial step for the synthesis of the triad involves the reaction of cyanuric chloride with Por-COOH in the presence of the base DIPEA at 0°C in THF (Scheme 2). TLC indicating the disappearance of the reactants monitored the reaction and the formation of the PorCOOH-triazine adduct **1**. The latter was not isolated but further reacted at room temperature with NH_2-BDP moiety affording the PorCOOH-triazine-BDP compound **2**. The third chlorine atom of cyanuric chloride was substituted by another NH_2-BDP moiety in an one-pot reaction at 65°C, resulting in the desired PorCOOH-$(BDP)_2$ product **3**, as confirmed by ^1H and ^{13}C NMR spectroscopy and MALDI-TOF spectrometry. In the ^1H NMR spectrum of PorCOOH-$(BDP)_2$ **3**, the signals of the aromatic H's *ortho* to the amino groups of Por-COOH moiety, after attachment to the triazine ring, are downfield displaced compared to those of free Por-COOH.

Photophysical properties

The optical absorption spectrum of **PorCOOH-$(BDP)_2$** in THF solution is shown in Figure 1. The spectrum of **PorCOOH-$(BDP)_2$** exhibits characteristic absorption bands for free-base porphyrin (strong Soret band: λ_{max} = 422 nm, weaker Q- bands: λ_{max}=552 nm, 596 nm and 652 nm). In addition to these bands, **PorCOOH-$(BDP)_2$** exhibits one more absorption band centered at 502 nm which is attributed to the π-π* transition of

BODIPY moiety.[33] The absorption spectrum of **PorCOOH-(BDP)$_2$** that shows the characteristic peaks of both porphyrin and BODIPY moieties, indicates negligible electronic interactions between porphyrin and BODIPY units in the ground state of the triad.

The absorption spectrum of **PorCOOH-(BDP)$_2$** adsorbed onto the TiO_2 film is similar (Figure 1) to the absorption spectrum in solution, but exhibits a small red shift and broadening, reflecting slight aggregation.

In Figure 2a the steady-state fluorescence spectrum of **PorCOOH-(BDP)$_2$** triad in THF solution is shown. It is known from the literature that BODIPY moieties exhibit a characteristic emission feature at about 510 - 550 nm.[21] Irradiation of the triad at 460 nm, which corresponds to the selective excitation of BODIPY moiety, results in emission peaks not only from the residual fluorescence of BODIPY moieties at 515 nm, with a lifetime of 2.24 ns, but also from the porphyrin constituent at 655 and 717 nm, with a lifetime of 8.23 ns. Additionally, the excitation spectrum of the triad, monitoring at the emission of the porphyrin constituent at 655 nm (Figure 2b), shows apart from the absorption features of porphyrin, a slightly enhanced BODIPY absorption feature at 502 nm. This is an indication of the possible existence of energy or electron transfer between BODIPY and porphyrin moieties, following excitation of BODIPY unit.

FT-IR spectroscopy

ATR-FTIR spectra of pure **PorCOOH-(BDP)$_2$** and **PorCOOH-(BDP)$_2$** adsorbed onto the TiO_2 surface were measured in order to explore the anchoring ability of **PorCOOH-(BDP)$_2$** on TiO_2[34] and shown in Figure 3. The FTIR spectrum of **PorCOOH-(BDP)$_2$** shows a characteristic strong absorption band at around 1694 cm^{-1}, which corresponds to the ν(C=O) stretching vibration of the carboxylic acid group, whereas two other absorption bands at around 1402 cm^{-1} and 1598 cm^{-1}, respectively, are also observed, corresponded to the symmetric stretching vibration $\nu_{sym}(COO^-)$ and the asymmetric stretching vibration $\nu_{asym}(COO^-)$ of the carboxylate group, respectively. However, in the ATR-FTIR spectrum of **PorCOOH-(BDP)$_2$**/TiO_2, the absorption band of the stretching vibration ν(C=O) of the carboxylic acid group is completely disappeared and a significant increase is observed in the band that correspond to the symmetric $\nu_{sym}(COO^-)$ and the asymmetric $\nu_{asym}(COO^-)$ vibration stretching of the carboxylate

group, at around 1402 cm^{-1} and 1598 cm^{-1}, respectively. The disappearance of ν(C=O) and increased intensity of ν_{sym}(COO-) and ν_{asym}(COO-) indicates that a proton is detached from the carboxylic acid group during the adsorption of the porphyrin onto the TiO_2 surface, leading to the bidentate binding of the carboxylate group to the TiO_2 surface.

XPS spectroscopy

We have also performed the X-ray photoelectron spectroscopy measurement for **PorCOOH-(BDP)$_2$** /TiO_2 to get more insight into the mode of the porphyrin binding on TiO_2 surface. The O 1s photoelectron spectrum (Figure 4) exhibits two distinct oxygen peaks at 530.3 and 532.5 eV. The oxygen atom on the TiO_2 surface gives the most intense peak at 530.3 eV and the moderate and broad peak at around 532.5 originates from the oxygen atoms of carboxylate groups that are attached onto the TiO_2 surface through the bidentate mode of attachment.[35]

Electrochemical properties

The electrochemical properties of the **PorCOOH-(BDP)$_2$** conjugate were investigated by cyclic and square wave voltammetry measurements in dichloromethane. The corresponding cyclic and square-wave voltammograms are presented in Figure 5 and Figure S5, respectively, while the redox data are collected in Table 2.

There are three oxidation processes, as shown in Figure S5, where the first oxidation wave occurs at E_{ox}^1 = +0.91 V vs SCE and corresponds to the first porphyrin-based oxidation, while the second and the third oxidation waves, placed at E_{ox}^2 = +1.12 V and E_{ox}^3 = +1.22 V vs SCE, respectively, are attributed to the overlapping second porphyrin and BODIPY-based oxidations, respectively. In addition, the reduction waves of the triad are reversible processes, observed at E_{red}^1 = -1.19 V and E_{red}^2 = -1.61 V vs SCE, and are due to the overlapping BODIPY and first porphyrin-based reductions and to the second porphyrin-based reduction, respectively.[21]

For the efficient electron injection from the excited state of porphyrin dye into the conduction band of TiO_2, the lowest unoccupied molecular orbital energy level of **PorCOOH-(BDP)$_2$,** which corresponds to its first reduction potential should be more negative than the conduction band edge of TiO_2 (-0.74 V vs SCE). The first reduction

potential of **PorCOOH-(BDP)$_2$** (E^1_{red} = -1.19 V vs SCE) is more negative than the conduction band edge of TiO_2; hence there is sufficient driving force for electron injection from the excited state of dye into the conduction band of TiO_2. For efficient regeneration of oxidized **PorCOOH-(BDP)$_2$** by I^- in the electrolyte, the highest occupied molecular orbital energy level of **PorCOOH-(BDP)$_2$,** which corresponds to its first oxidation potential, should be lower than the potential of redox couple I_3^-/I^- (0.2 V vs SCE) in the electrolyte. The first oxidation potential (E^1_{ox} = 0.91 V vs SCE) of **PorCOOH-(BDP)$_2$** is more positive than the redox potential of I_3^-/I^- in electrolyte, implying that regeneration of the oxidized **PorCOOH-(BDP)$_2$** is energetically feasible.

Theoretical Calculations.

DFT calculations at the B3LYP/6-31G(d) level of theory were employed for further exploring the molecular and electronic structure of the final compound.

The gas phase geometry optimized structure of **PorCOOH-(BDP)$_2$** is depicted in Figure 6, while the optimized coordinates are provided in Table S1 in Supporting Information. From the optimized structure we observe that the triazine ring is almost co-planar with the two bridging phenyl group of the BODIPY units and the bridging phenyl group of the porphyrin as well. The three peripheral units (BODIPY units and porphyrin) form a perpendicular framework with respect to the triazine ring, extending the central π-conjugated system. We can also notice that the phenyl and the 2,4,6-trimethylphenyl groups are perpendicular to the BODIPY and to the porphyrin ring respectively.

The electron density map and the corresponding energies of the frontier molecular orbitals (FMOs) of **PorCOOH-(BDP)$_2$** are presented in Figure 7. The LUMO and LUMO+1 are very close in energy and their electron density is predominantly located on the porphyrin unit, with some additional contributions on the benzoic acid group and the bridging phenyl group. The HOMO is spread over the porphyrin unit, while the HOMO-1 is entirely localized on the BODIPY unit. Consequently, **PorCOOH-(BDP)$_2$** could be described as a "push-pull" 2D-π-A system (D: donor, A: acceptor) system with potential to act as sensitizer in DSSCs. The electron density distributions on HOMO-1, LUMO, and LUMO+1 favor intramolecular electron transfer. More precisely, upon photoexcitation, electron transfer possibly occurs from the donor (BODIPY unit) to the

acceptor (porphyrin unit) through the triazine π-conjugated system. The fact that the LUMOs orbital are located on the porphyrin unit and on the anchoring carboxylic acid group successfully promotes the electron injection into the TiO_2 conduction band.

For the optimized structure of **PorCOOH-(BDP)$_2$** the corresponding HOMO and LUMO energies, the HOMO-LUMO gap and the dipole moment are listed in Table 3. The HOMO-LUMO gap was calculated in CH_2Cl_2 solution and was found to be 2.67 eV. This value is similar to the experimentally observed HOMO-LUMO gap from our electrochemistry experiments (Table 2).

The UV-vis absorption spectra of **PorCOOH-(BDP)$_2$** have also been calculated at the TD-DFT/B3LYP level (Figure S1). At small wavenumbers we can observe that the compound exhibits a high intensity band with five peaks. While at larger wavenumbers two low intensity bands appeared around 540 and 580 nm. Furthermore, the intensity band peaks are found to be at 375 nm (3.31 eV), 389 nm (3.19 eV) and 397 nm (3.12 eV), and 410 nm (3.03 eV), 422 nm (2.94 eV), 542 nm (2.29 eV) and 579 nm (2.14 eV).

Photovoltaic properties

We have optimized the performance of DSSC by investigating the immersion time of TiO_2 electrode during the sensitization process. We have investigated the effect of immersion time of TiO_2 electrode into the porphyrin dye solution on the photovoltaic performance of the DSSCs. The TiO_2 electrode was sensitized by **PorCOOH-(BDP)$_2$** THF solution for 1-12 h and we found that maximum photovoltaic performance was observed when the immersion time was 4h, beyond which the value of PCE starts to decrease slightly with the increase in immersion time, which can be reorganized by an increase in porphyrin aggregation with increasing immersing time.[36] It is well known that dye molecules which are only chemisorbed on TiO_2 by either chelating, monodense esteric linkage, bidentate bridging or hydrogen bonding, can inject electrons into the conduction band of TiO_2, contribute to the J_{sc} value of the cell. Therefore, the excess amount of dye, which does not contributes to the current generation, may be present either in multi-layers or physisorbed on TiO_2. The difference in the immersion time for maximal PCE value can be explained as a trade off between the effect of the extent of porphyrin adsorption and that of porphyrin aggregation, which adversely affect PCE

value. We have only discussed the photovoltaic properties of the DSSC prepared in optimized conditions.

Figure 8a and 8b show the current – voltage characteristics under illumination (100 mW/cm^2) and incident photon to current efficiency (IPCE) for DSSC based on **PorCOOH-(BDP)$_2$** (sensitization time 4h) (device A) and the photovoltaic parameters are summarized in Table 4. The optimized DSSC showed a PCE value of 5.09% with J_{sc}= 10.86 mA/cm^2, V_{oc} = 0.67 V and FF = 0.70. The IPCE spectrum closely resembles the absorption spectrum of the **PorCOOH-(BDP)$_2$** sensitized TiO_2 photoelectrode.

In most of the DSSCs, the TiO_2 has been used as photoelectrode, but the major drawback associated with the use of TiO_2 is the random transport of the electrons, which causes the electron – hole recombination process, and, hence, affects the photovoltaic performance of the DSSC.[37] The problem about how to improve the PCE value of the DSSC could be overcome by designing a photoanode with efficient transport pathway from the injected charge carriers to the external circuit. Several kinds of photoanode materials have been employed, such as doped TiO_2,[38] metal/metal oxide – TiO_2 hybrid[39] and TiO_2 – carbon materials,[40] to improve and reduce the electron transport and recombination, respectively.

Graphene, a single layer of sp^2 – bonded carbon atoms, is a promising material for transparent electrodes based on 2 dimensional (2D) planer structure and the unique electronic properties, which include excellent optical transparency and high carrier mobility.[41] Among many chemically modified graphene composites, the reduced graphene oxide (rGO) is most used in nanoelectronics. Significant efforts have been devoted to using graphene composites for improving the overall performance of photovoltaic devices such as organic photovoltaic devices and DSSCs.[42] Due to, not only its remarkable electrical conduction, but the matching conduction band of TiO_2 and graphene serves as the charge transport medium to enhance the electron transfer from the conduction band to the FTO. Thus, integration of TiO_2 with graphene derivatives could be highly promising in order to improve the photovoltaic performance of TiO_2. Many reports have demonstrated that the incorporation of graphene onto TiO_2 was an efficient way for enhancing the photovoltaic performance of DSSCs.[43] We have used rGO/TiO_2 photoanode to improve the PCE of DSSC sensitized with **PorCOOH-(BDP)$_2$**.

Figure S6 shows the SEM images of TiO_2 and rGO/TiO_2 electrodes. There are more pores in TiO_2 electrode as compared to rGO/TiO_2, and we assume rGO penetrates into the TiO_2 and pores are filled by the rGO during the spin coating process and form rGO/TiO_2 composite. The surface area of rGO/TiO_2 and TiO_2 are about 51.96 m^2/g and 52.08 m^2/g, respectively, which are nearly same indicating that rGO/TiO_2 electrode, will not improve the dye adsorption. Moreover, the TiO_2 nanoparticles can easily attached to the penetrated rGO during the spin casting, as a result of the electrostatic charges. This complete and continuous contact between components will facilitate the photoexcited electron transfer from the TiO_2 to the rGO conducting layer and attributed to the enhanced value of Jsc and FF as discussed in later part.

The interaction between the TiO_2 and rGO in the prepared photoanodes was investigated by UV-visible diffuse reflectance spectroscopy. As shown in Figure S7, pure TiO_2 film show typical and intense absorption in the UV region (less than 380 nm), resulting from the electron transitions from the valance band to conduction band. However, when rGO was spin coated onto the TiO_2, i.e. rGO/TiO_2 film showed a broad band absorption in the visible region, which could be ascribed to the existence of reduced graphene oxide in the rGO/TiO_2 film. Moreover, introduction of rGO onto the TiO_2 film, the hybrid film display a red shift of the absorption edge, which indicates the band gap of rGO/TiO_2 has a tendency of narrowing. On the basis of the optical absorption, we assume that during the spin coating of GO onto TiO_2 from the aqueous solution, the GO penetrates onto the TiO_2 and after the hydrothermal treatment rGO/TiO_2 hybrid film was formed. On the basis of above results, it was proposed that the Ti-O-C bond between TiO_2 and rGO was formed[44].

To further improve the PCE value of the DSSC sensitized by **PorCOOH-(BDP)$_2$** dye (device B), we have employed a modified photoanode, i.e. rGO/TiO_2 (as described in experimental part). It is obvious that, device B shows a PCE value of 6.20%, due to high J_{sc} value and FF (Figure 8, Table 4).

The recombination of injected photoinduced charge carrier from the excited state of dye into the semiconductor is crucial because it would significantly influence photoelectrochemical properties and DSSC performance. The recombination of photoinduced charge carriers (electrons and holes), releases the energy in the form of

photoluminescence (PL). Hence a lower PL intensity indicates less charge recombination. We have recorded the PL spectra of TiO_2 and rGO/TiO_2 films and shown in Figure S8. A broad peak with maximum emission at 575 nm was observed for both TiO_2 and rGO/TiO_2 films. The TiO_2 film showed higher PL intensity due to the rapid recombination of photoinduced charge carriers. The PL intensity decreased when a thin film of rGO was introduced onto TiO_2 film. This is mainly attributed to the formation of a Schottky barrier at the rGO/TiO_2 interface, which acts as electron could sink to effectively prevent the charge carrier recombination. Moreover, the rGO could acts as bridge to accelerate the electron transfer from the TiO_2 to the electrode.

The enhancement in the J_{sc} and FF may be attributed to the higher electron transfer efficiency driven by the Schottky barrier (formed due to the difference in energy level between TiO_2 and rGO) and the improved interface contact in the dye/rGO/TiO_2 of the DSSC. The potential of rGO was found to be higher than that of TiO_2, indicating a potential drop to drive electrons from rGO to TiO_2 in this junction. In device B, the quasi Fermi level of the rGO is shifted upward after the injection of the photogenerated electrons from the LUMO level of dye molecules, which were adsorbed onto rGO film through π-π interactions. As a result, on dye/rGO/TiO_2 interface, the electrons can easily be transported from the LUMO of the dye to the conduction band of TiO_2, driven by the internal potential difference, and consequently enhancing the J_{sc} value. Therefore, we assume that a Schottky barrier formed between rGO and TiO_2 play an important role in enhancement of transport efficiency photogenerated electrons from the dye.

To understand the different J_{sc} values of the DSSCs fabricated by different photoanodes, i.e. TiO_2 and rGO/TiO_2 hybrid, the IPCE spectra were measured. Figure 8b shows the IPCE spectra of devices A and B. The IPCE values at each wavelength are higher for the device B as compared to device A. In general, the IPCE value of the DSSC depends on the light harvesting efficiency of dye sensitized photoanode, the efficiency of electron injection, and the efficiency of collecting photoinjected electrons at the FTO surface. The IPCE spectra of both DSSCs closely resemble the absorption spectra of **PorCOOH-(BDP)$_2$** adsorbed onto the TiO_2 surface, indicating that J_{sc} and IPCE values mainly originate from the light harvesting of dye adsorbed by the photoanode films upon light illumination. The increase in the values of IPCE is consistent with the J_{sc} values.

It is well known that the J_{sc} value of DSSC is associated with the number of injected electrons collected by the FTO, while V_{oc} value corresponds to the difference between the quasi Fermi level of TiO_2 under illumination and Nernst potential of I_3^- / I^- redox couple in the electrolyte. Almost the same value of V_{oc} for both devices, reveals that the incorporation of rGO does not influence the Fermi level of rGO/TiO_2, which is consistent with the other reports.[45] On the other hand, the J_{sc} value has been significantly improved with the incorporation of rGO layer between dye and TiO_2, which is attributed to the collection of electrons by the FTO electrode. Two possible factors may contribute to the increase in the number of electrons by the incorporation of rGO layer: (i) increasing the amount of dye sensitizer adsorbed onto the photoanode and thus increasing the excited electrons from dye sensitizer to the conduction band of TiO_2, and (ii) enhancing the electron transfer from TiO_2 to the FTO surface. We have measured the amount of dye loading for both photoanodes using dye desorption method and found that the amount of dye loading is almost the same, indicating that the introduction of rGO layer does not increase the number of photoinjected electrons from dye to the conduction band of TiO_2. In other words, increase in the J_{sc} value may be attributed to the enhancement of electron transfer from TiO_2 to photoanode due to the formation of Schottky barrier in the device B.[46]

Electrochemical impedance spectroscopy (EIS) is a useful tool to investigate the interfacial charge transfer processes occurring in the DSSCs, such as charge recombination at the TiO_2/dye/electrolyte, electron transport in the TiO_2 electrode, electron transfer at the counter electrode, and the I_3^- transport in the electrolyte.[47] We have carried out the EIS data by subjecting the DSSC under illumination (100 mW/cm^2) and using a forward bias at the V_{oc} of the DSSC (under the condition of no current), for better manifesting the process at the TiO_2/dye/electrolyte of the device under operation. The Nyquist plots of EIS of the DSSCs under different conditions are shown in Figure 9 and exhibit clearly three semicircles in the frequency range, which are investigated (0.1 Hz to 100 kHz). The small semicircle, in the right side of the spectrum, occurs in the lowest frequency range of 0.1 Hz to 1 Hz and corresponds to the charge Nernst diffusion in the electrolyte. The larger semicircle, in middle frequency range, is related to the charge transfer processes at the TiO_2/dye/electrolyte interface and another smaller

semicircle, in the left side of the spectrum, at even higher frequencies, is associated with the charge transfer process at the platinum counter electrode/electrolyte interface. The DSSC with rGO/TiO_2 photoelectrode shows a smaller middle semicircle, thus, a lower charge transfer resistance (R_{ct}) than that for TiO_2 photoelectrode. The smaller R_{ct} of DSSC based on rGO/TiO_2, the more efficient generation of electrons and thus, the larger electron collection at the TiO_2/rGO/dye/electrolyte interface, which results in higher J_{sc} and PCE values. We have also estimated the value of chemical capacitance (C_μ) for both the DSSCs and complied in table 5. The value of C_μ is higher for the device B as compared to device A, consistent with the trends reported in literature[43d]. As shown in Bode phase plots (Figure 9b), the characteristic peak for electron transport process of rGO/TiO_2 photoanode is shifted to lower frequency region compared to pristine TiO_2 photoanode. Every shift of the peak from high frequency to low frequency reveals a more rapid electron transport process, because the characteristic frequency (f_c) in the middle frequency region can be related to the inverse of electron lifetime (τ_n) in TiO_2 film according to the equation: $\tau_n = 1/2\pi f_c$. The calculated electron lifetimes of TiO_2 and rGO/TiO_2 DSSCs were found to be 23 and 32 ms, respectively. This further confirms that incorporation of rGO layer accelerate the electron transfer from TiO_2 to the photoelectrode, leading to the reduction of the recombination of injected electrons with I_3^- in the redox couple. We have also plotted the Nyquist plots of EIS in dark at dc voltage equivalent to the open circuit voltage of the devices and similar shapes of the plots as under illumination, have been observed (not shown) and estimated the charge recombination resistance (R_{rec}) of both devices (complied in table 5). It was found that the R_{rec} is higher for device B as compared to the one of device A. The higher value of R_{rec} indicates that the recombination of injected electrons into the conduction band of TiO_2 with I_3^- in the redox couple is suppressed. The electron transport time (τ_d) and charge collection efficiency (η_{cc}) were estimated from the expressions: $\tau_d / \tau_n = R_{ct} / R_{rec}$, and $\eta_{cc} = 1 - \tau_d/\tau_n$, respectively. The values of R_{ct}, R_{rec}, τ_n, τ_d and η_{cc} are summarized in Table 5. The values of electron transport time and charge collection efficiency are significantly lower and higher, respectively, for the devices A and B,

providing an explanation of the higher values of J_{sc} and PCE for device B as compared to the ones of device A.

It can be seen from Table 4 that FF has also been increased from 0.70 (device A) to 0.75 (device B). It is well known that the FF of DSSC is affected by the series resistance arising from internal resistance of the device.[48] The increase in the FF for device B may be attributed to the reduction of recombination of the injected electron with the redox couple due to the formation of conductive layer, when rGO is inserted between TiO_2 and dye.

Due to the excellent electrical conduction, the two dimensional rGO bridges behave as an electron transfer channel, which can transport the photoinduced electron quickly. Under the illumination, the electrons from the photoexcited dye. Because the TiO_2 is anchored with two dimension rGO, and rGO is homogeneous in the system, the injected electrons are captured by the rGO without any obstruction. The collected electrons can transport from TiO_2 to the conductive surface quickly and effectively through the rGO bridges, and adverse reactions (recombination and back reaction) are suppressed, leading to the enhancement in FF.

Conclusions

We have synthesized a porphyrin-BODIPY triad **PorCOOH-(BDP)$_2$**, in which metal free porphyrin unit is covalently bridged with two BODIPY chromophores by 1,3,5 triazine moiety. The photophysical and electrochemical measurements of **PorCOOH-(BDP)$_2$** along with theoretical calculations reveal that it has suitable energy levels for efficient electron injection and regeneration processes, when used as sensitizer for DSSCs. The DSSCs based on pristine TiO_2 (device A) and rGO/TiO_2 (device B) photoanodes sensitized by this porphyrin-BODIPY triad, resulted in PCE values of 5.17% and 6.20%, respectively. The higher PCE value for device B has been attributed to the formation of a Schottky barrier between rGO and TiO_2 which facilitate the electron transport towards the FTO surface more efficiently, due to the internal field as evidenced by the reduce of charge transfer resistance, and electron transport time. This PCE value for DSSC based on that porphyrin-BODIPY triad is higher than the one of single

porphyrin moiety. Furthermore, these results provide new directions and ideas for further improvement.

Supporting Information

Cartesian coordinates, theoretically calculated UV-Vis spectrum, ^{1}H NMR and ^{13}C NMR spectra, square-wave voltammogram and MALDI-TOF spectrum of triad **PorCOOH-(BDP)$_2$** and also SEM images, UV-Vis absorption and photoluminescence spectra of TiO_2 and rGO/TiO_2 films.

Acknowledgements

Financial support from the European Commission (FP7-REGPOT-2008-1, Project BIOSOLENUTI No. 229927) is greatly acknowledged, as well Special Research Account from the University of Crete. This research has also been co-financed by the European Union (European Social Fund) and Greek national funds (Heraklitos II) through the Operational Program "Education and Lifelong Learning" of the National Strategic Reference Framework Research Funding Program (THALIS-UOA-MIS 377252).

References

1. (a) M. Liang and J. Chen, *Chem. Soc. Rev.*, 2013, **42**, 3453 (b) B. E. Hardin, H. J. Snaith and M. D. McGeHee, *Nat. Photonics*, 2012, **6**, 162 (c) C. Risko, M. D. McGehee and J. L. Bredas, *Chem. Sci.*, 2011, **2**, 1200 (d) Y. Bai, J. Zhang, D. Zhou, Y. Wang, M. Zhang and P. Wang, *J. Am. Chem. Soc.*, 2011, **133**, 11442 (e) B. O'Regan and M. Grätzel, *Nature*, 1991, **353**, 737 (f) X. Yang, M. Yanagida and L. Han, *Energy Environ. Sci.*, 2013, **6**, 54 (g) A. Hagfeldt, G. Boschloo, L. Sun, L. Kloo and H. Pettersson, *Chem. Rev.*, 2010, **110**, 6595 (h) J. Wu, Y. Xiao, G. Yue, Q. Tang, J. Lin, M. Huang, Y. Huang, L. Fan, Z. Lan, S. Yin and T. Sato, *Adv. Mater.*, 2012, **24**, 1884
2. (a) M. Zhang, Y. Wang, M. Xu, W. Ma, R. Li, P. Wang, *Energy Environ. Sci.,* 2013, **6**, 2944–2949 (b) X. Ren, S. Jiang, M. Cha, G. Zhou, Z. S. Wang, *Chem. Mater.,* 2012, **24**, 3493–3499 (c) J. Liu, Y. Numata, C. Qin, A. Islam, X. Yang, L. Y. Han, *Chem. Commun.,* 2013, **49**, 7587–7589
3. (a) C. L. Wang, Y. C. Chang, C. M. Lan, C. F. Lo, E. W. G. Diau, C. Y. Lin, *Energy Environ. Sci.*, 2011, **4**, 1788–1795, (b) L.-L. Li and E. W.-G. Diau, *Chem. Soc. Rev.*, 2013, **42**, 291, (c) Y. Wang, B. Chen, W. Wu, X. Li, W. Zhu, H. Tian, and Y. Xie, *Angew. Chem. Int. Ed*., 2014, **53**, 10779
4. (a) T. Bessho, S. M. Zakeeruddin, C. Y. Yeh, E. W. G. Diau, M. Grätzel, *Angew. Chem.*, 2010, **122**, 6796–6799, *Angew. Chem. Int. Ed.,* 2010, **49**, 6646–6649, (b) T. Ripolles-Sanchis, B. Guo, H. Wu, T. Pan, H. Lee, S. Raga, F. Santiago, J. Bisquert, C. Y. Yeh, E. W. G. Diau, *Chem. Commun.*, 2012, **48**, 4368–4370, (c) C. Wang, C. Lan, S. Hong, Y. Wang, T. Pan, C. Chang, H. Kuo, M. Kuo, E. W. G. Diau, C. Y. Lin, *Energy Environ. Sci.*, 2012, **5**, 6933–6940.
5. (a) S. Mathew, A. Yella, P. Gao, R. H. Baker, B. F. E. Curchod, N. A. Astani, I. Tavernelli, U. Rothlisberger, M. K. Nazeeruddin, M. Grätzel, *Nat. Chem.*, 2014, **6**, 242–247, (b) A. Yella, C. L. Mai, S. M. Zakeeruddin, S. N. Chang, C. H. Hsieh, C. Y. Yeh, M. Grätzel, *Angew. Chem.,* 2014, **126**, 3017–3021, *Angew. Chem. Int. Ed.*, 2014, **53**, 2973–2977
6. M. Tanka, S. Hayashi, S. Eu, T. Umeyama, Y. Matano, H. Imahori, *Chem. Comm.*, 2007, 2069-2071
7. (a) Q. Wang, W. M. Campbell, E. E. Bonfantani, K. W. Jolley, D. L. Officer, P. J. Wash, K. Gordon, R. Humphry-Baker, M. K. Nazeeruddin, M. Gratzel, *J. Phys. Chem. B*, 2005, **109**, 15397-15409, (b) W. M. Campbell, K. W. Jolley, P. Wagner, K. Wagner, P. J. Walsh, K. C. Gordon, S. M. Lukas, M. K. Nazeeruddin, Q. Wang, M. Gratzel, D. L. Officer, *J. Phys. Chem.*, 2007, **111**, 11760-11762
8. (a) Z. Kostereli, T. Ozdemir, O. Buyukcakir and E. U. Akkaya, *Org. Lett.*, 2012, **14**, 3636–3639, (b) S. Atilgan, T. Ozdemir and E. U. Akkaya, *Org. Lett*., 2010, **12**, 4792–4795, (c) S. Kolemen, O. A. Bozdemir, Y. Cakmak and E. U. Akkaya, *Chem. Sci.*, 2011, **2**, 949–954, (d) Shin H. Choi, K. Pang, K. Kim, D. G.

Churchill, *Inorg. Chem.*, 2007, **46**, 10564-10577, (e) K. Kim, S. H. Choi, J. Jeon, H. Lee, J. O. Huh, J. Yoo, J. T. Kim, C.-H. Lee, Y. S. Lee, D. G. Churchill, *Inorg. Chem.*, 2011, **50**, 5351–5360

9. C. Qin, A. Mirloup, N. Leclerc, A. Islam, A. El-Shafei, L. Han, and R. Ziessel, *Adv. Energy Mater.* 2014, DOI: 10.1002/aenm.201400085
10. (a) T. Zhang, X. Zhu, W.-K. Wong, H.-L. Tam and W.-Y. Wong, *Chem.– Eur. J.*, 2013, **19**, 739–748, (b) T. K. Khan, M. Bröring, S. Mathur and M. Ravikanth, *Coord. Chem. Rev.*, 2013, **257**, 2348–2387, (c) T. K. Khan and M. Ravikanth, *Tetrahedron*, 2012, **68**, 830–840, (d) A. N. Kursunlu, *RSC Adv.*, 2014, **4**, 47690-47696, (e) C. Jiao, L. Zhu and J. Wu, *Chem. Eur. J.*, 2011, **17**, 6610 – 6614
11. B. Brizet, A. Eggenspiller, C. P. Gros, J.-M. Barbe, C. Goze, F. Denat and P. D. Harvey, *J. Org. Chem.*, 2012, **77**, 3646–3650
12. C. Y. Lee, J. T. Hupp, *Langmuir*, 2010, **26**, 3760–3765
13. T. Lazarides, S. Kuhri, G. Charalambidis, M. K. Panda, D. M. Guldi and A. G. Coutsolelos, *Inorg. Chem.*, 2012, **51**, 4193–4204
14. (a) H. Zhong, E. Xu, D. Zeng, J. Du, J. Sun, S. Ren, B. Jiang and Q. Fang, *Org. Lett.*, 2008, **10**, 709, (b) J.-W. Kang, D.-S. Lee, H.-D. Park, Y.-S. Park, J.-W. Kim, W.-I. Jeong, K.-M. Yoo, K. Go, S.-H. Kim and J.-J. Kim, *J. Mater. Chem.*, 2007, **17**, 3714; (c) A. P. Kulkarni, C. J. Tonzola, A. Babel and S. A. Jenekhe, *Chem. Mater.*, 2004, **16**, 4556.
15. (a) C. A. M. Afonso, N. M. T. Lourenco¸ and A. A. Rosatella, *Molecules*, 2006, **11**, 81; (b) X. Qi, S. K. Kim, S. J. Han, L. Xu, A. Y. Jee, H. N. Kim, C. Lee, Y. Kim, M. Lee, S.-J. Kima, J. Yoon, *Tetrahedron Lett.*, 2008, **49**, 261-264; (c) Xin Qi, S. K. Kim, S. J. Han, L. Xu, A. Y. Jee, H. N. Kim, C. Lee, Y. Kim, M. Lee, S.-J. Kim, J. Yoon, *Supramol. Chem.*, 2009, **21**, 455-464.
16. (a) S. Ren, D. Zeng, H. Zhong, Y. Wang, S. Qian and Q. J. Fang, *Phys. Chem. B*, 2010, **114**, 10374, (b) H. Zhong, H. Lai and Q. Fang, *J. Phys. Chem. C*, 2011, **115**, 2423
17. J. Liu, K. Wang, X. Zhnag, C. Li, X. You, *Tetrahedron*, 2013, **69**, 190–200
18. A. Luechai, J. Gasiorowski, A. Petsom, H. Neugebauer, N. S. Sariciftci and P. Thamyongkit, *J. Mater. Chem.*, 2012, **22**, 23030
19. G. D. Sharma, G. E. Zervaki, P. A. Angaridis, T. N. Kitsopoulos, and A. G. Coutsolelos, *J. Phys. Chem. C*, 2014, **118**, 5968−5977
20. (a) G. E. Zervaki, E. Papastamatakis, P. A. Angaridis, V. Nikolaou, M. Singh, R. Kurchania, T. N. Kitsopoulos, G. D. Sharma and A. G. Coutsolelos, *Eur. J. Inorg. Chem.*, 2014, 1020–1033, (b) G. E. Zervaki, M. S. Roy, M. K. Panda, P. A. Angaridis, E. Chrissos, G. D. Sharma and A. G. Coutsolelos, *Inorg. Chem.*, 2013, **52**, 9813−9825, (c) G. E. Zervaki, P. A. Angaridis, E. N. Koukaras, G. D. Sharma and A. G. Coutsolelos, *Inorg. Chem. Front.*, 2014, **1**, 256–270

21. T. Lazarides, G. Charalambidis, A. Vuillamy, M. Réglier, E. Klontzas, G. Froudakis, S. Kuhri, D. M. Guldi, and A. G. Coutsolelos, *Inorg. Chem.*, 2011, **50**, 8926–8936
22. M. G. Walter, C. C. Wamser, J. Ruwitch, Y. Zhao, D. Braden, M. Stevens, A. Denman, R. Pi, A. Rudine and P. J. Pessiki, *J. Porphyrins Phthalocyanines,* 2007, **11**, 601-612
23. G. W. T. Gaussian 03, M. J. Frisch, H. B. Schlegel, G. E. Scuseria, M. A. Robb, J. R. Cheeseman, J. A. Montgomery, T. Vreven, K. N. Kudin, J. C. Burant, J. M. Millam, S. S. Lyengar, J. Tomasi, V. Barone, B. Mennucci, M. Cossi, G. Scalmani, N. Rega, G. A. Petersson, H. Nakatsuji, M. Hada, M. Ehara, K. Toyota, R. Fukuda, J. Hasegawa, M. Ishida, T. Nakajima, Y. Honda, O. Kitao, H. Nakai, M. Klene, X. Li, J. E. Knox, H. P. Hratchian, J. B. Cross, V. Bakken, C. Adamo, J. Jaramillo, R. Gomperts, R. E. Stratmann, O. Yazyev, A. J. Austin, R. Cammi, C. Pomelli, J. W. Ochterski, P. Y. Ayala, K. Morokuma, G. A. Voth, P. Salvador, J. J. Dannenberg, V. G. Zakrzewski, S. Dapprich, A. D. Daniels, M. C. Strain, O. Farkas, D. K. Malick, A. D. Rabuck, K. Raghavachari, J. B. Foresman, J. V. Ortiz, Q. Cui, A. G. Baboul, S. Clifford, J. Cioslowski, B. B. Stefanov, G. Liu, A. Liashenko, P. Piskorz, I. Komaromi, R. L. Martin, D. J. Fox, T. Keith, M. A. Al-Laham, C. Y. Peng, A. Nanayakkara, M. Challacombe, P. M. W. Gill, B. Johnson, W. Chen, M. W. Wong, C. Gonzalez, J. A. Pople, Gaussian 03 (Revision D.01), Gaussian Inc., Wallingford, CT, 2004.
24. L. S. W. Kohn, *J. Phys. Rev.*, 1965, **140**, A1133.
25. A. D. Becke, *Phys Rev A*, 1988, **38**, 3098-3100.
26. C. T. Lee, W. T. Yang and R. G. Parr, *Phys Rev B*, 1988, **37**, 785-789
27. M. Cossi, V. Barone, R. Cammi and J. Tomasi, *Chem Phys Lett*, 1996, **255**, 327-335.
28. D. A. Z. Zhurko, G. A. ChemCraft 1.6; Plimus: San Diego, CA. Available at http://www.chemcraftprog.com
29. N.I. Kovtyukhova, P.J. Ollivier, B.R. Martin, T.E. Mallouk, S.A. Chizhik, E.V. Buzaneva, A.D. Gorchinskiy, Chem. Mater. 11 (1999) 771–778
30. D. W. P. M. Löwik, C. R. Lowe, *Eur. J. Org. Chem.,* 2001, 2825-2839
31. (a) M. B. Steffensen, E. E. Simanek, *Org. Lett.* 2003, **5**, 2359-2361. (b) W. Zhang, E. E. Simanek, *Org. Lett.,* 2000, **2**, 843-845
32. (a) T. Carofiglio, A. Varotto, U. Tonellato, *J. Org. Chem.,* 2004, **69**, 8121-8124. (b) K. Ichihara, Y. Naruta, *Chem. Lett.,* 1995, 631-632. (c) T. Carofiglio, E. Lubian, I. Menegazzo, G. Saielli, A. Varotto, *J. Org. Chem.,* 2009, **74**, 9034-9043.
33. J. Karolin, L. B. A. Johansson, L. Strandberg, T. Ny, *J. Am. Chem. Soc.*, 1994, **116**, 7801–7806

34. (a) P.-A. Bouit, M. Marszalek, R. Humphry-Baker, R. Viruela, E. Orti, S. M. Zakeeruddin, M. Gratzel, J. L. Delgado, N. Martin, *Chem. Eur. J.*, 2012, **18**, 11621–11629, (b) A. Abbotto, N. Manfredi, C. Marinzi, F. De Angelis, E. Mosconi, J.-H. Yum, Z. Xianxi, M. K. Nazeeruddin, M. Grätzel, *Energy Environ. Sci.*, 2009, **2**, 1094–1101, (c) N. Lu, J.-S. Shing, W.-H. Tu, Y.-C. Hsu, J. T. Lin, *Inorg. Chem.*, 2011, **50**, 4289–4294
35. (a) H. Imahori, Y. Matsubara, H. Iijima, T. Umeyama, Y. Matano, S. Ito, M. Niemi, N. V. Tkachenko, H. Lemmetyinen, *J. Phys. Chem. C*, 2010, **114**, 10656–10665, (b) A. Kira, Y. Matsubara, H. Iijima, T. Umeyama, Y. Matano, S. Ito, M. Niemi, N. V. Tkachenko, H. Lemmetyinen, H. Imahori, *J. Phys. Chem. C*, 2010, **114**, 11293–11304, (c) R. B. Ambre, G.-F. Chang, M. R. Zanwar, C.-F. Yao, E. W.-G. Diau, C.-H. Hung, *Chem. Asian J.*, 2013, **8**, 2144 –2153
36. (a) H. Imahori, S. Hayashi, H. Hayashi, A. Oguro, S. Eu, T. Umeyama, Y. Matano, *J. Phys. Chem. C*, 2009, **113**, 18406, (b) H. Imahori, S. Kang, H. Hayashi, M. Haruta, H. Kurata, S. Isoda, S. E. Canton, Y. Infahsaeng, A. Kathiravan, T. Pascher, P. Chabera, A. P. Yartsev, V. Sundstrçm, *J. Phys. Chem. A*, 2011, **115**, 3679
37. (a) J. van de Lagemaat, N. G. Park and A. J. Frank, *J. Phys. Chem. B*, 2000, **104**, 2044–2052, (b) N. Kopidakis, N. R. Neale, K. Zhu, J. van de Lagemaat and A. J. Frank, *Appl. Phys. Lett.*, 2005, **87**, 202106.
38. (a) H. Tian, L. Hu, C. Zhang, L. Mo, W. Li, J. Sheng, S. Dai, *J. Mater. Chem.*, 2012, **22**, 9123−9130, (b) F. Huang, Q. Li, G. J. Thorogood, Y.-B. Cheng, R. A. Caruso, *J. Mater. Chem.*, 2012, **22**, 17128−17132
39. (a) J. Du, J. Qi, D. Wang, Z. Tang, *Energy Environ. Sci.*, 2012, **5**, 6914−6918, (b) T. Chen, G. H. Guai, C. Gong, W. Hu, J. Zhu, H. Yang, Q. Yan, C. M. Li, *Energy Environ. Sci.*, 2012, **5**, 6294−6298, (c) K. Kakiage, T. Tokutome, S. Iwamoto, T. Kyomen, M. Hanaya, *Chem. Commun.*, 2013, **49**, 179−180
40. Y. H. Jang, X. Xin, M. Byun, Y. J. Jang, Z. Lin, D. H. Kim, *Nano Lett.*, 2011, **12**, 479−485
41. (a) K. S. Novoselov, A. K. Geim, S. V. Morozov, D. Jiang, Y. Zhang, S. V. Dubonos, I. V. Grigorieva, A. A. Firsov, *Science*, 2004, **306**, 666, (b) S. Stankovich, D. A. Dikin, G. H. B. Dommett, K. M. Kohlhaas, E. J. Zimney, E. A. Stach, R. D. Piner, S. T. Nguyen, R. S. Ruoff, *Nature*, 2006, **442**, 282, (c) H. Y. Mao, Y. H. Lu, J. D. Lin, S. Zhong, A. T. S. Wee, W. Chen, *Prog. Surf. Sci.*, 2013, **88**, 132
42. (a) D. W. Chang, H.-J. Choi, A. Filer, J.-B. Baek, *J. Mater. Chem. A,* 2014, **2**, 12136-12149, (b) J. Liu, M. Durstock and L. Dai, *Energy Environ. Sci.*, 2014, **7**, 1297–1306, (c) Z. Yin, J. Zhu, Q. He, X. Cao, C. Tan, H. Chen, Q. Yan and H. Zhang, *Adv. Energy Mater.*, 2014, **4**, 1–19, (d) Y. H. Hu, H. Wang, B. Hu,

ChemSusChem, 2010, **3**, 782 – 796, (e) J. D. Roy-Mayhew, I. A. Aksay, *Chem. Rev.,* 2014, **114**, 6323–6348

43. (a) Y. B. Tang, C. S. Lee, J. Xu, Z. T. Liu, Z. H. Chen, Z. He, Y. L. Cao, G. Yuan, H. Song, L. Chen, L. Luo, H. M. Cheng, W. J. Zhang, I. Bello, S. T. Lee, *ACS Nano,* 2010, **4**, 3482-3488, (b) J. Fan, S. Liu, J. Yu, *J. Mater. Chem.*, 2012, **22**, 17027-17036, (c) B. Tang, G. Hu, *Journal of Power Sources*, 2012, **220**, 95-102, (d) K. T. Dembele, G. S. Selopal, R. Milan, C. Trudeau, D. Benetti, A. Soudi, M. M. Natile, G. Sberveglieri, S. Cloutier, I. Concina, F. Rosei, A. Vomiero, *J. Mater. Chem. A*, **3**, 2580 – 2588.
44. (a) H. Zhang, X. Lv, Y. Li, Y. Wang, J. Li, *ACS Nano*, 2010, **4**, 380-386, (b) W. Fan, Q. Lai, Q. Zhang, Y. Wang, *J. Phys. Chem. C*, 2011, **115**, 10694-10701.
45. N. Yang, J. Zhai, D. Wang, Y. Chen, L. Jiang, *ACS Nano*, 2010, **4**, 887−894
46. J. Song, Z. Yin, Z. Yang, P. Amaladass, S. Wu, J. Ye, Y. Zhao, W.-Q. Deng, H. Zhang, X.-W. Liu, *Chem. Eur. J.*, 2011, **17**, 10832 –10837
47. Q. Wang, J. Moser, M. Gratzel, *J. Phys. Chem. B*, 2005, **109**, 14945–14953
48. (a) N. Satoh, T. Nakashima, K. Yamamoto, *J. Am. Chem. Soc.*, 2005, **127**, 13030, (b) L. Han, A. Fukui, Y. Chiba, A. Islam, R. Komiya, N. Fuke, N. Koide, R. Yamanaka, M. Shimizu, *Appl. Phys. Lett.*, 2009, **94**, 013305, (c) Y. Chiba, A. Islam, Y. Watanabe, R. Komiya, N. Koide, L. Han, *Jpn. J. Appl. Phys.*, 2006, **45**, L638

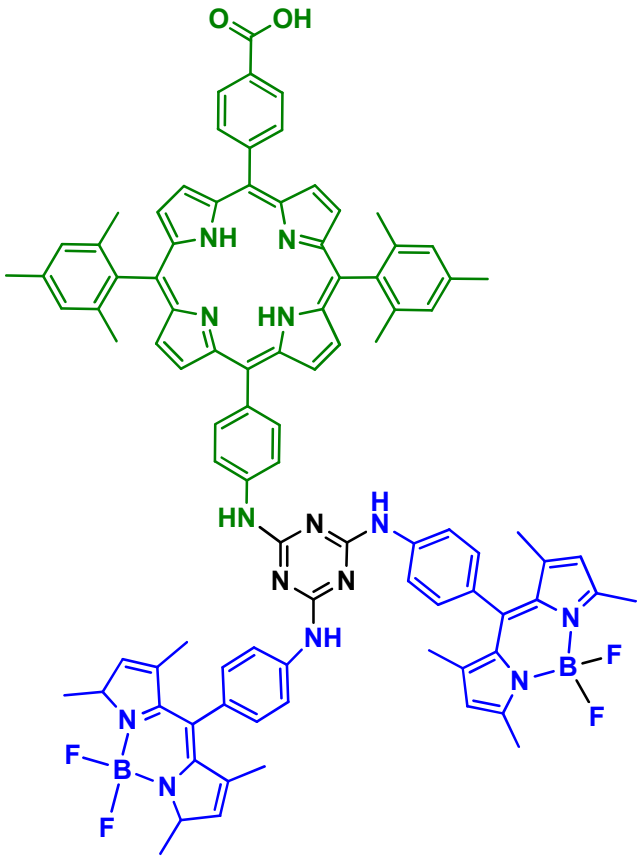

Scheme 1. Triad porphyrin chromophore **PorCOOH-(BDP)$_2$**

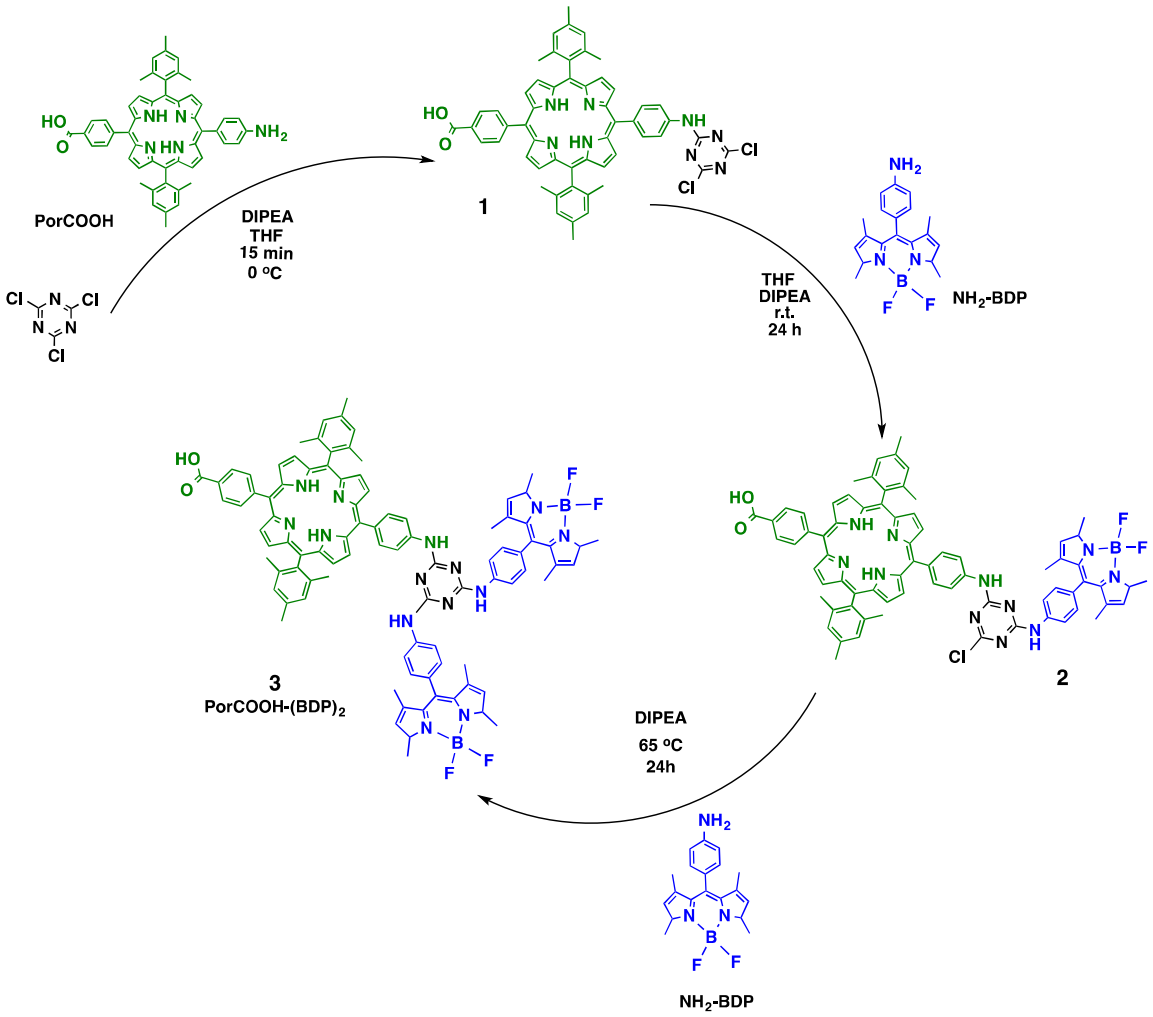

Scheme 2 Synthetic route for preparation of porphyrin **PorCOOH-(BDP)$_2$**

Table 1. Summary of spectroscopic data for the **PorCOOH-(BDP)$_2$** .

Compound	Absorption λ_{max} / nm (ε / $\times 10^{-3}$ $M^{-1}.cm^{-1}$) in solution[a]	Emission λ_{max} / nm, in solution[b]	τ / ns
PorCOOH-(BDP)$_2$	420 (351.2), 502 (10.2), 550 (9.6), 592 (5.9), 650 (7.0)	515, 655, 717	0.08 (5.71%) 2.24 (30 %) 8.23 (64.3%)

[a] measured in CH_2Cl_2 at 298K
[b] measured in THF at 298K

Table 2. Electrochemical data[a], and calculated band gaps E_g^{elec} for the **PorCOOH-(BDP)$_2$** .

Compound	E^1_{ox}, V	E^2_{ox}, V	E^3_{ox}, V	E^1_{red}, V	E^2_{red}, V	HOMO – LUMO, V
PorCOOH-(BDP)$_2$	0.91	1.12	1.22	-1.19	-1.61	2.10

[a]The observed potentials are measured in CH_2Cl_2 vs. SCE.

Table 3. DFT calculated properties of **PorCOOH-(BDP)$_2$**: HOMO and LUMO energies, HOMO-LUMO gap and dipole moment (μ).

Compound	HOMO (eV)	LUMO (eV)	HL (eV)	μ(D)
B3LYP	-5.13	-2.46	2.67	8.28

Table 4. Photovoltaic parameters of DSSC based on **PorCOOH-(BDP)$_2$** porphyrin dye using pristine TiO_2 (device A) and rGO/TiO_2 (device B) photoanodes.

Device	J_{sc} (mA/cm^2)	Voc (V)	FF	PCE (%)
A	10.86	0.68	0.70	5.17
B	12.52	0.66	0.75	6.20

Table 5. EIS parameters of DSSC based on **PorCOOH-(BDP)$_2$** porphyrin dye using pristine TiO_2 (device A) and rGO/TiO_2 (device B) photoanodes

Device	R_{rec} (Ω)	C_μ (F) x10^{-5}	R_{ct} (Ω)	τ_n (ms)	τ_d (ms)	η_{cc}
A	38	6.05	36	23	20	0.53
B	56	11.90	24	32	14	0.70

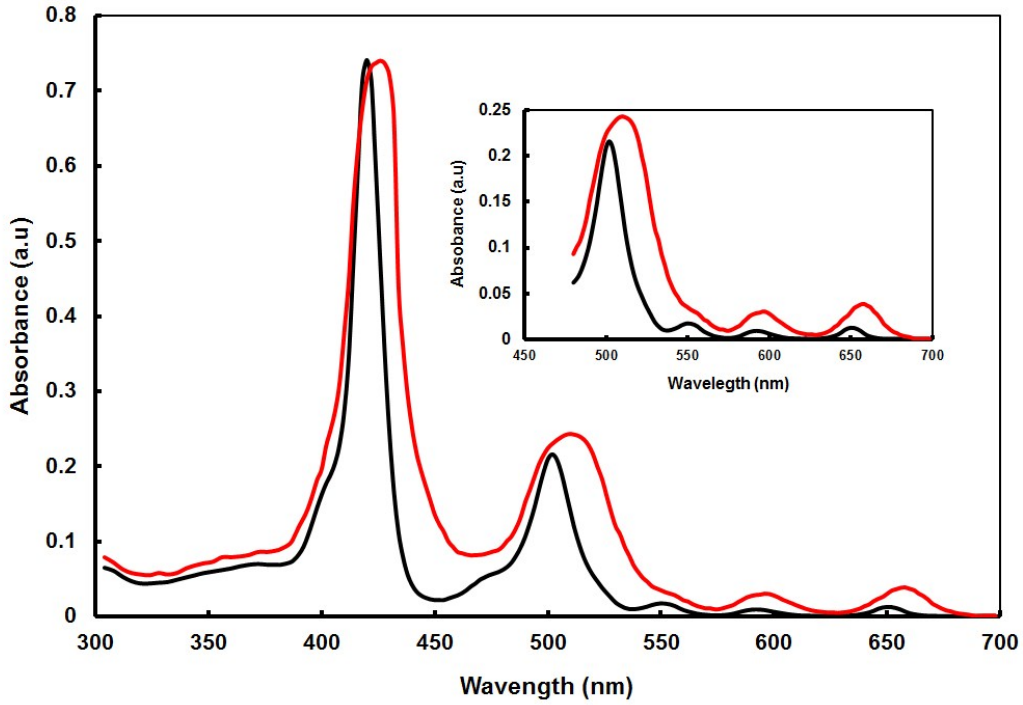

Figure 1. Normalized UV-visible absorption spectra of **PorCOOH-(BDP)$_2$** in THF solution (black color line) and adsorbed onto TiO_2 film (red color line)

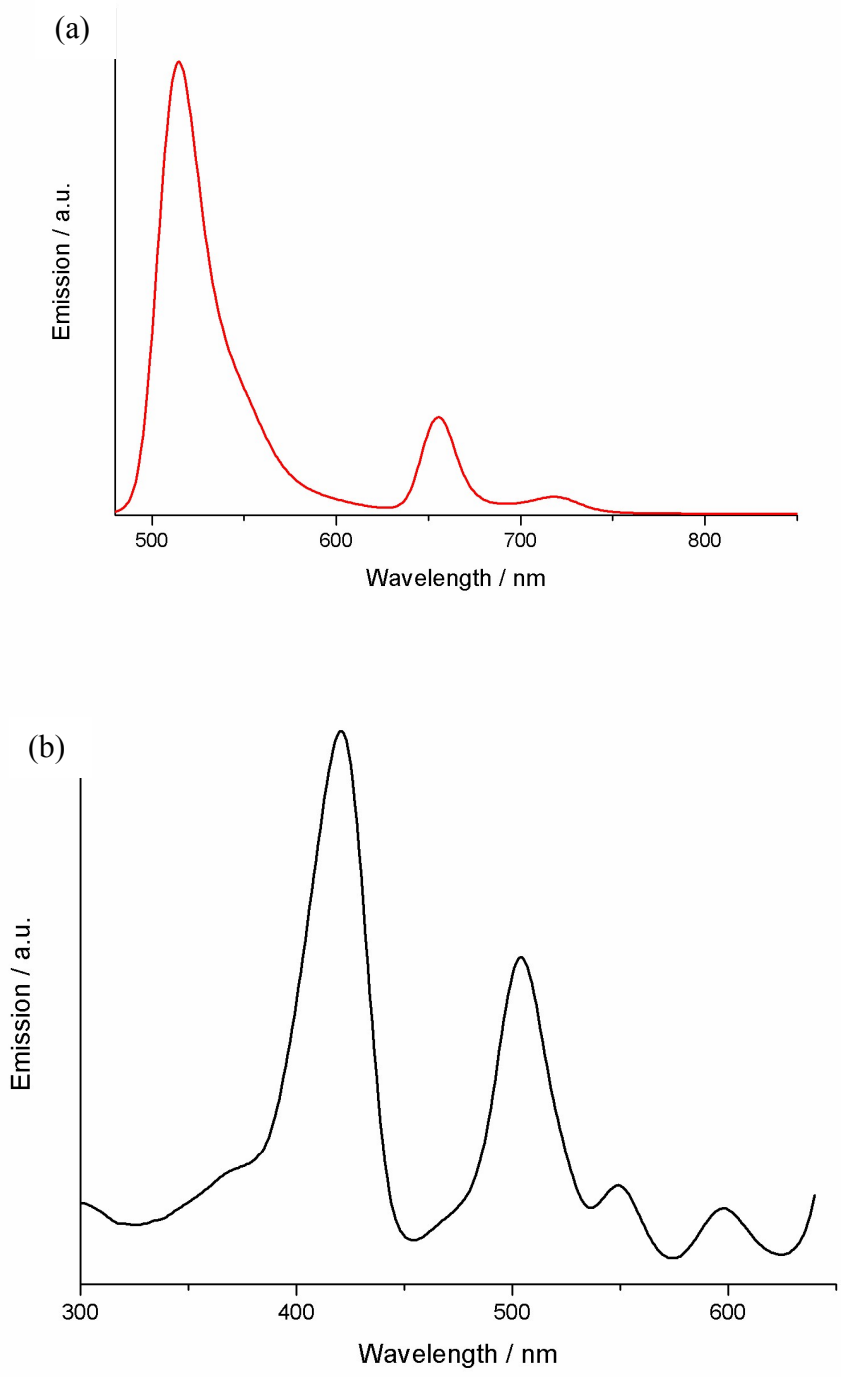

Figure 2. (a) Isoabsorbing emission spectrum of triad **3** in THF solution, at room temperature, upon selective excitation of BODIPY constituent at 460 nm. (b) Room temperature excitation spectrum of **3** monitoring at 655 nm.

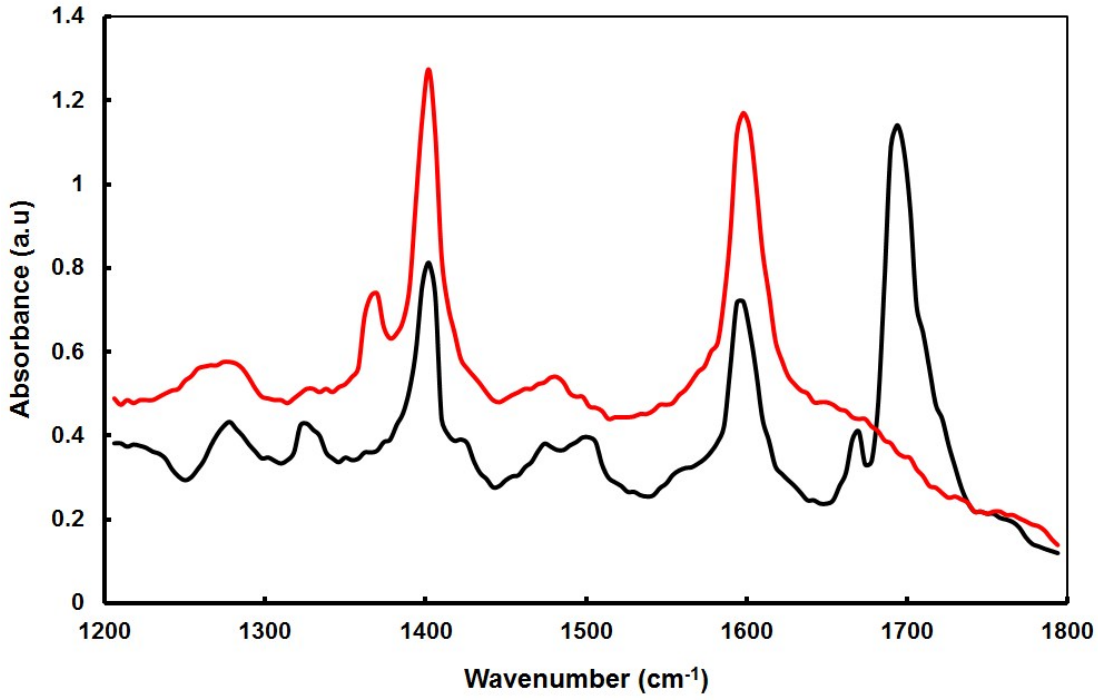

Figure 3. ATR-FTIR spectra of **PorCOOH-(BDP)$_2$** (black color line) and **PorCOOH-(BDP)$_2$** /TiO_2 (red color line) films

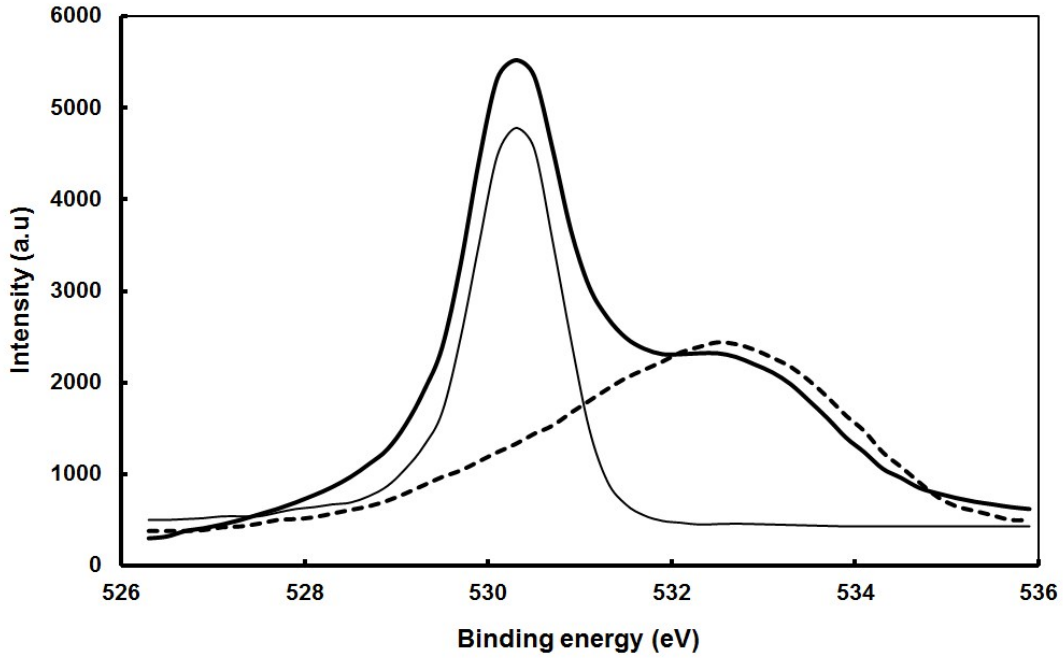

Figure 4. XPS O 1s spectrum of **PorCOOH-(BDP)$_2$** /TiO_2

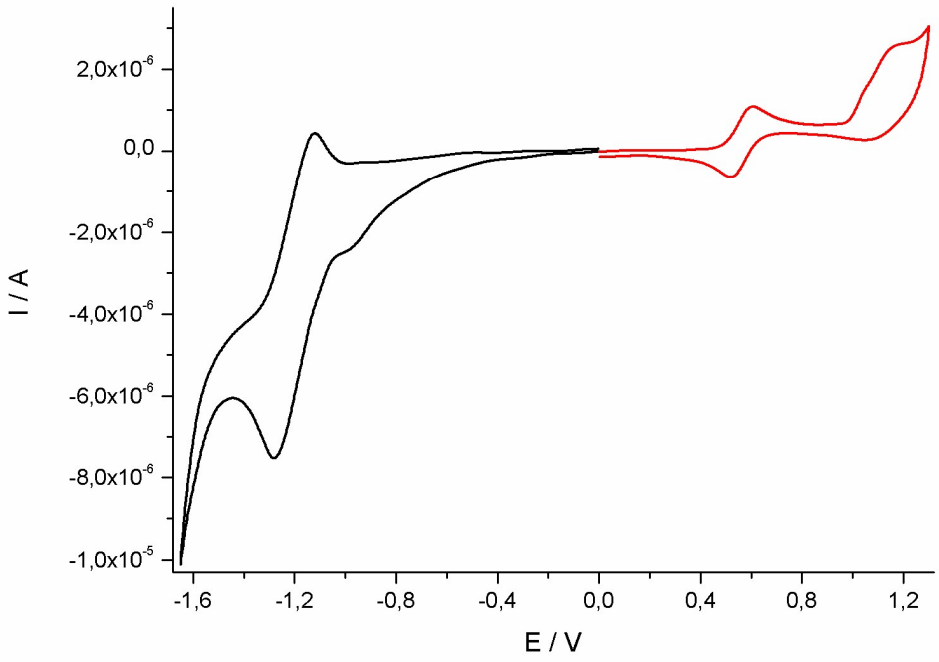

Figure 5. Cyclic voltamogram of **PorCOOH-(BDP)$_2$** in CH_2Cl_2 vs SCE. The ferrocene/ferrocenium (Fc/Fc^+) redox couple wave is observed at 0.56 V vs SCE.

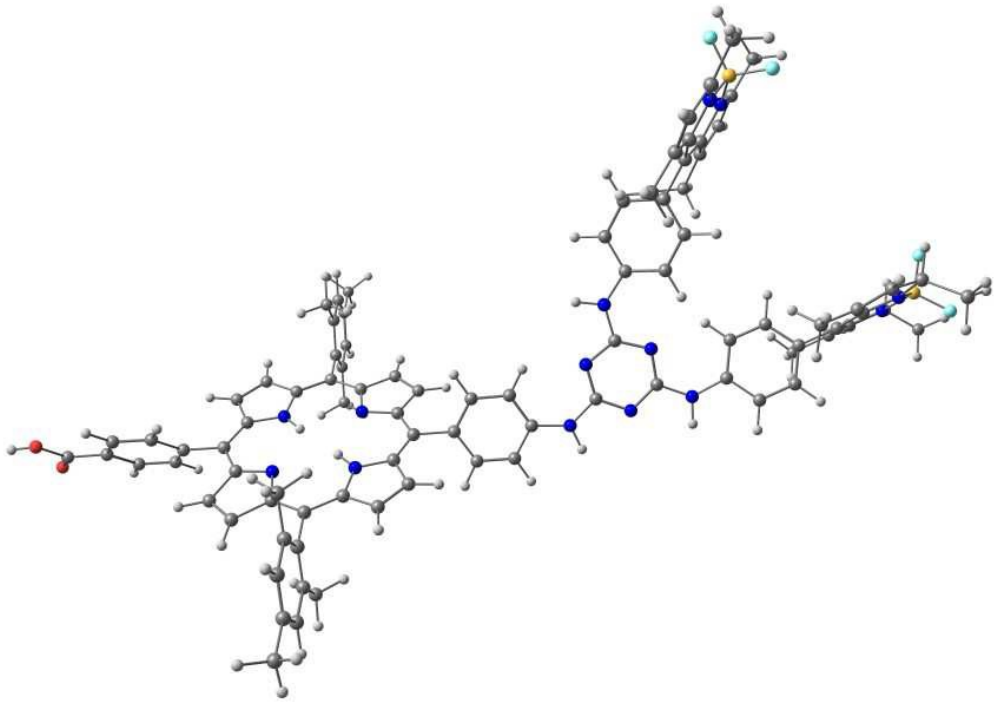

Figure 6. Gas phase geometry optimized structure of **PorCOOH-(BDP)$_2$**. Carbon, nitrogen, hydrogen, oxygen, fluoro and boron atoms correspond to grey, blue, white, red, light blue and yellow spheres, respectively.

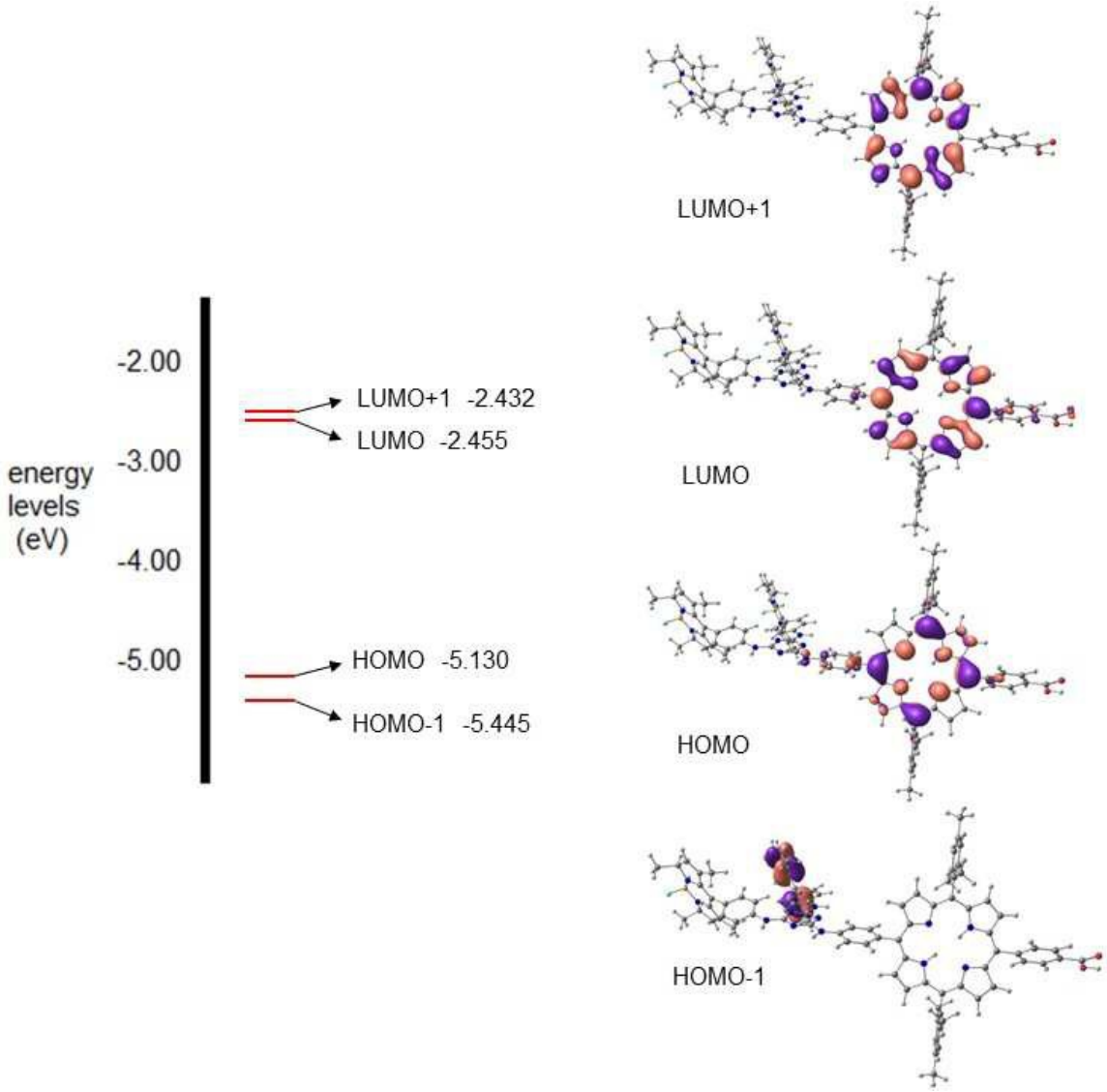

Figure 7. Frontier molecular orbitals of **PorCOOH-(BDP)$_2$** with the corresponding energy levels.

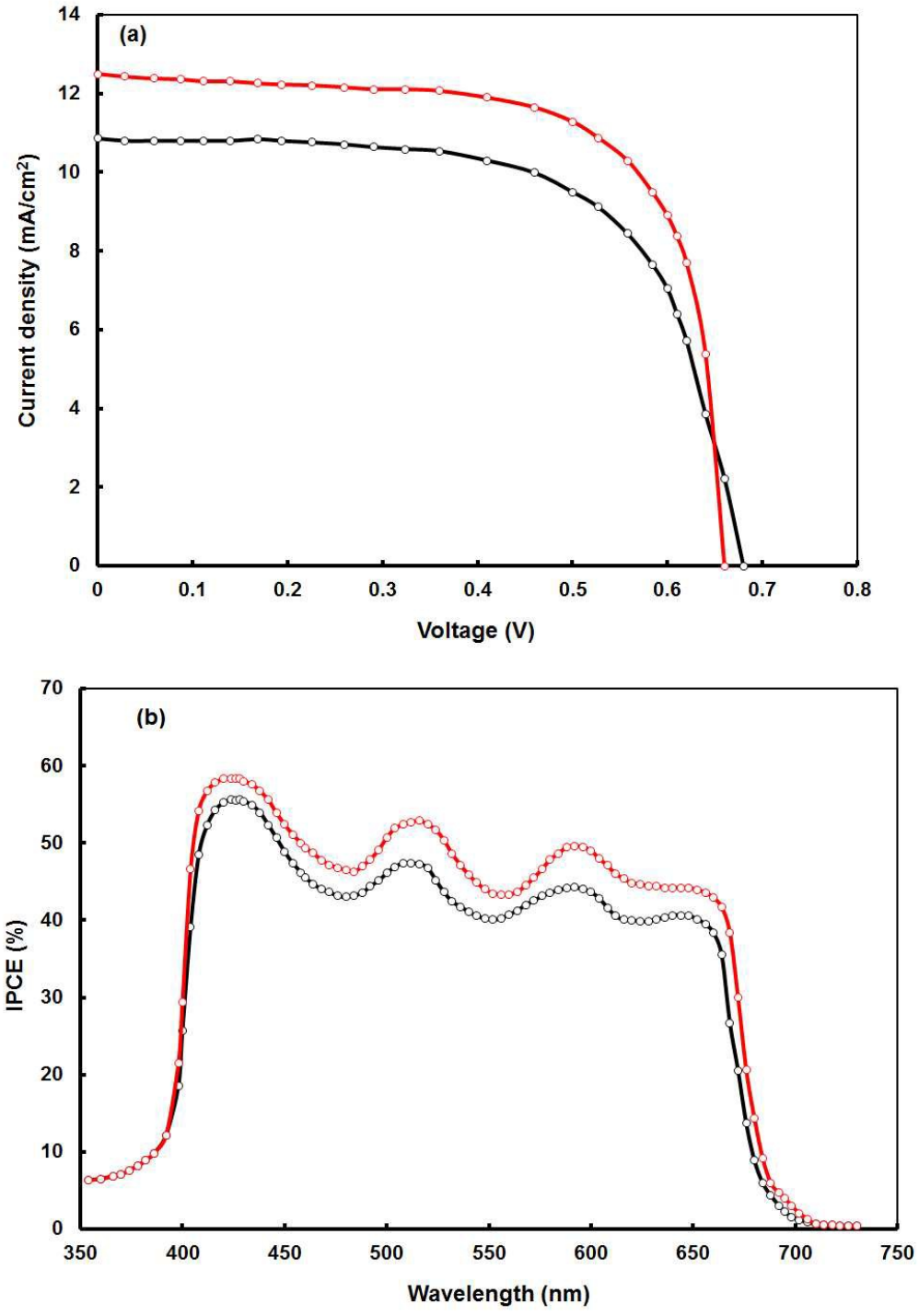

Figure 8. (a) Current-voltage (J-V) characteristics and (b) IPCE spectra of device A (black color line) and device B (red color line)

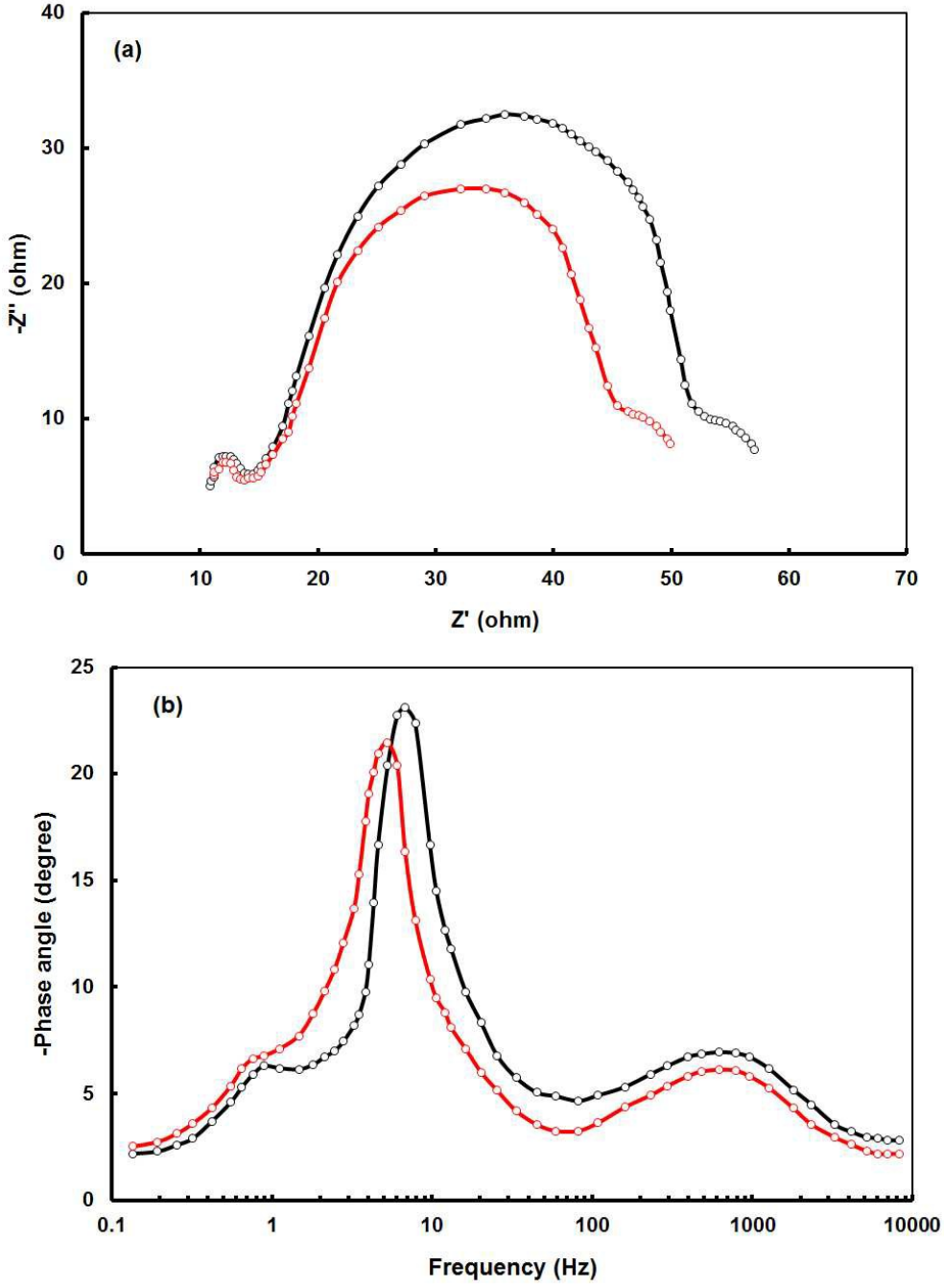

Figure 9. EIS data (a) Nyquist plots and (b) Bode phase plots under illumination for the device A (black color line) and device B (red color line).